Graphical Abstract

In-Situ Characterization of Microgel Monolayers: Controlling Isostructural Phase Transitions for Homogeneous Crystal Drying Patterns

Antonio Rubio-Andrés, Delfi Bastos-González, Miguel Angel Fernandez-Rodriguez

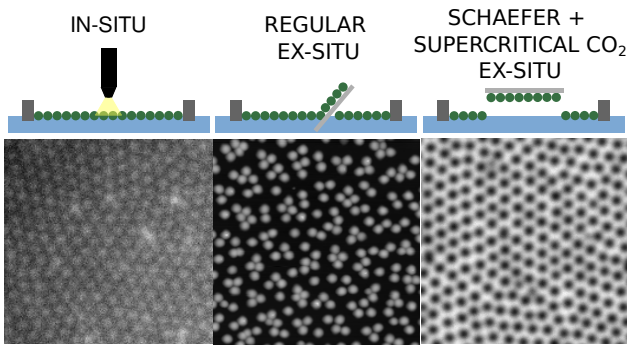

Highlights

In-Situ Characterization of Microgel Monolayers: Controlling Isostructural Phase Transitions for Homogeneous Crystal Drying Patterns

Antonio Rubio-Andrés, Delfi Bastos-González, Miguel Angel Fernandez-Rodriguez

- Isostructural Phase Transition (IPT) is only observed in ex-situ measurements.
- Capillary and Marangoni Forces can be combined to create a 'zero-force' environment.
- IPT occurs as a result of the capillary forces arising upon drying of the monolayer.
- Adhesion forces can be estimated from microgel compression curves at the interface.
- Supercritical drying avoid IPT, unlocking highly compressed and ordered monolayers.

In-Situ Characterization of Microgel Monolayers: Controlling Isostructural Phase Transitions for Homogeneous Crystal Drying Patterns

Antonio Rubio-Andrés, Delfi Bastos-González, Miguel Angel Fernandez-Rodriguez*

Laboratory of Surface and Interface Physics, Biocolloid and Fluid Physics Group, Department of Applied Physics, Faculty of Sciences, University of Granada, Granada, 18071, Spain

Abstract

The self-assembly of microgels at fluid interfaces and transfer to solid substrates has proven valuable in fields like photonics, plasmonics, and nanofabrication. However, this process is constrained by the isostructural phase transition (IPT) that occurs under sufficiently high compression, disrupting the monolayer order. Understanding the mechanisms driving IPT is crucial to extend their applicability to a wider range of interparticle distances. We tackle this problem by studying the monolayer conformation via in-situ microscopy at the interface. We monitored the microgel monolayer throughout the different stages of the deposition onto a solid substrate. We found that neither the compression at the interface nor the capillary forces arising from the receding meniscus during the deposition triggered the IPT. In fact, the still wet deposited monolayers do not exhibit IPT regardless of the compression of the monolayer. Instead, the IPT occurs during the drying of the wet deposited monolayers, particularly when the capillary force overcomes the adhesion force. Additionally, we found a new mechanism to modulate the interparticle distance by light-induced Marangoni forces. Instead, IPT arises from capillary forces generated during the drying of the water film after the monolayer is transferred. We propose a theoretical model to estimate the adhesion force between the microgels and the substrate based on the compression curve of the monolayer. Furthermore, we suggest a novel method combining a Langmuir-Schaefer deposition with supercritical drying to fully prevent the IPT, resulting also in a new tool to study an otherwise inaccessible regime with highly compressed monolayers. Our findings advance the understanding of soft colloidal self-assembly at fluid interfaces and expand their applications, enabling the creation of larger substrates with highly ordered self-assembled microgel monolayers with tunable interparticle distance.

Keywords: Soft Colloidal Lithography, Self-assembly, Microgels, In-Situ characterization, Capillary Forces, Homogeneous Drying, Marangoni

1. Introduction

The homogeneous drying of nanoparticle films is a hot research topic due to its wide range of applications, such as in coatings, nanofabrication, and photonics [1, 2, 3, 4]. For such applications, nanoparticle films are typically deposited from bulk suspensions. While this method allows for a rapid and scalable production of nanoparticle films, there are common drawbacks such as the coffee-ring effect [5, 6], or the difficulty in fine tuning the properties of the nanoparticle films, such as the ordering or the spacing between nanoparticles, critical for colloidal lithography applications [7, 8, 9]. To circumvent these issues, there is another way to fabricate nanoparticle films by taking advantage of their ability to self-assemble into monolayers at liquid interfaces [10]. The monolayers can be deposited in a controlled way on substrates, such as in Lanmguir-Blodgett depositions. The properties of the resulting monolayers can be precisely tuned by altering the morphology and/or chemical composition of the nanoparticles, i.e. by engineering the interaction potential during the self-assembly at the liquid interface. Nevertheless, the capillary forces during the monolayer transfer and drying are a critical problem, since they tend to cause nanoparticle aggregation and disorder within the monolayer [11]. While alternative methodologies involving the use of water/hexane interfaces can mitigate to some extent this problem [12], the range of nanoparticle

*Corresponding author

Email address: mafernandez@ugr.es (Miguel Angel Fernandez-Rodriguez)

compositions and interparticle distances is still limited by their interactions at the liquid interface and the capillary forces during transfer and drying.

A promising alternative to overcome the disorder during transfer an drying involves adding "softness" to the nanoparticles, such as in the case of microgels [13, 14, 15]. Microgels are soft nanoparticles composed of crosslinked polymer networks where the monomer and co-monomers can impart responsiveness to different stimuli, such as thermoresponsiveness when poly-N-isopropylacrylamide (pNIPAM) is used as monomer. This reversible response to temperature arises from hydrogen bonds stabilizing the polymeric network, above $\simeq 32^{\circ}$ C (volume phase transition temperature, VPPT), the thermal energy κT is in the order of the hydrogen bonds, causing the expulsion of water molecules and the collapse of the microgel [16]. Moreover, the usual synthesis by precipitation polimerization is able to produce in a reliable way significantly monodisperse microgel dispersions, useful for their self-assembly into homogeneous crystals. Their softness and thus the degree to which the microgels can collapse/swell can be easily controlled by the crosslinking density during the synthesis, where the microgels develop a Gaussian profile of crosslinking density, with a denser core and a less crosslinked corona. When microgels adsorb at a liquid interface, they stretch as much as possible to reduce the surface tension, only limited by the inner elasticity of the polymeric network [17]. As a result, the microgels adsorbed at the interface adopt a 'fried-egg' shape with a stretched portion adsorbed at the interface and a still well solvated portion in the aqueous sub-phase [18, 19, 20]. This distinctive morphology allows microgels to easily self-assemble into regular monolayers at liquid interfaces, with the capillary attraction and steric repulsion between microgels being the main ingredients in the process [14]. Furthermore, the softness of the microgels enables fine control over interparticle distances by compressing the elastic monolayer at the interface. This softness plus the gelation of the monolayer facilitate their transfer onto solid substrates while preserving their ordering. These advantages have been exploited to develop the Soft Colloidal Lithography (SCL) technique, where self-assembled microgel monolayers act as colloidal masks for different purposes, such as producing vertically aligned nanowires, assisting in the deposition of other nanoparticles, or fabricating diffraction patterns [21, 14, 22, 23].

In 2016, we described that microgels in a self-assembled monolayer at liquid interfaces undergo an isostructural phase transition (IPT) upon compression [24]. At low compressions, microgels arrange into hexagonal close-packed (hcp) arrays with all microgels in contact through the portions adsorbed and stretched at the interface. Upon further compression, some of those stretched portions begin to collapse and microgels start interacting also via the solvated portions in the aqueous sub-phase, resulting in a loss of order, i.e. the onset of the IPT. This order is eventually recovered when enough compression is applied to the monolayer, leading to all microgels being in a new more compressed hcp order where all microgels are in contact via their solvated portions in the sub-phase. Therefore, there is a window of interparticle distances that we cannot access so far for a particular microgel since the onset of the IPT causes disorder of the monolayer. In this way, it is crucial to understand the underlying mechanisms driving the IPT in developing strategies to prevent it. This IPT has traditionally been attributed to the failure of the stretched portions of the microgels at the interface under compression of the monolayer [24]. However, verifying this hypothesis requires in-situ studies that examine the conformation of microgel monolayers upon compression at liquid interfaces.

In this regard, different approaches have been employed to gain further insights about the in-situ behavior of microgels at interfaces. Neutron scattering techniques, together with simulations, have provided valuable information about the out-of-plane conformation of microgels [25, 26]. The recently developed in-situ atomic force microscopy (AFM) enabled the possibility of reconstructing the actual 3D shape of microgels at an water/oil interface [27, 28]. These techniques, however, do not provide information about the arrangement of the microgels within the monolayer and thus can not help to directly explore the IPT. Freeze fracture shadow casting (FreSCa) Cryo-Sem offers the possibility of imaging the monolayer after freezing it [29, 18]. However, its complexity prevented an extensive use of this technique. Very recently, significant progress has been made in imaging microgel monolayers in-situ using optical microscopy [30, 31]. A particular interesting approach is the coupling of a Langmuir balance with optical microscopy to study in-situ the behavior of microgel monolayers at liquid interfaces, comparing it to their ex-situ structure after the deposition onto a solid substrate. With this method, the behavior of the microgel monolayer at different compression stages can be easily monitored. Notably, their results revealed that the IPT does not seem to occur at the liquid interface but rather upon the transfer process onto a solid substrate [30, 31, 32]. Nevertheless, a comprehensive study of all steps involved in the deposition and drying process is missing, which would lead to a better understanding of when, where, and why the IPT occurs.

In this work, we use an optical microscope coupled to a Langmuir trough to systematically study the differences between microgel monolayers at liquid interfaces, i.e. in-situ, and deposited monolayers, i.e. ex-situ. We present a comprehensive experimental study supported by theory and simulations to elucidate the exact mechanism behind the IPT. In the process, we provide a new tool to control the interparticle distance by light-driven Marangoni flows. Finally, we propose a novel deposition method to fully prevent the IPT at high surface pressures. This approach expands the range of application of the SCL technique and offers a new way to study the high pressure compression regime, being able to switch on and off the IPT at will.

2. Results and discussion

Our chosen system is a conventional pNIPAM microgel with 4.8 %mol crosslinking density, using KPS as initiator of the precipitation polymerization. The initiator provides a negative charge to the microgel when dispersed in Milli-Q water, with an electrophoretic mobility $\mu_e = -2.23 \pm 0.02\,\mu mcm/Vs$. The average hydrodynamic diameter and polydispersity index measured by DLS at $24°\,C$ is $653 \pm 25\,nm$, with a PDI of 0.08. At $50°\,C$, well above the VPPT, the microgel shrinks down to $400 \pm 10\,nm$. The swelling ratio, defined as the quotient between the sizes of the microgel in its expanded and collapsed state, is $\frac{D_{h,25°C}}{D_{h,50°C}} \simeq 1.6$. For the study at the water/air interface, we add isopropanol (IPA) to the microgel dispersion as spreading agent, in a 4:1 water:IPA ratio, and deposit them on a Langmuir trough to obtain a self-assembled microgel monolayer. In Figure 1, we show the response of the monolayer to lateral compression, i.e. the compression curve. As the motorized barriers of the Langmuir trough compress uni-axially the monolayer, the surface pressure Π increases and the distance between microgels decreases, thereby reducing the area per particle A_p. Usually, this kind of data is obtained via ex-situ measurements, where the monolayer is transferred onto a solid substrate while compressing the interface, producing a continuous gradient of Π [24, 21, 33, 34, 35]. The monolayer is subsequently imaged ex-situ, and each position on the substrate is correlated with its corresponding Π, from which A_p can be extracted. In order to create a reference point in the substrate to help in relating Π, measured in-situ, and A_p, measured ex-situ, a common practice is to suddenly open the barriers at the end of the experiment to create a point that can be easily found during the ex-situ imaging. When only this information was available, it was common to assume that the conformation of the deposited microgel, i.e. ex-situ, was the same as the monolayer at the liquid interface, i.e. in-situ. This assumption considers that the forces experienced by the microgels during the transfer and drying process are not higher than the steric repulsion between microgels. Nevertheless, the process of the monolayer deposition involves a receding meniscus on a substrate [36], and its subsequent drying. Aiming to assess the possible differences between in-situ and ex-situ images of the monolayer, we compare their respective compression curves and monolayer configuration in Figure 1.

Differences Between Ex-situ and In-situ Characterization Methods

In order to represent both curves, corresponding to two different experiments with the same pNIPAM microgel, we took respectively in-situ and ex-situ images to track the microgels and obtain the A_p for each image. The slight differences between both curves can be ascribed to small differences in the initial conditions. While we keep a strict criteria to make the experiments as reproducible as possible (see Materials & Methods), in the best scenario the Langmuir balance is still sensitive to the initial zeroing of Π, and even more to the deposition of the microgels with the spreading agent. Nevertheless, since both compression curves are rather similar, we can infer that indeed the experimental conditions were comparable enough between both experiments. Upon the initial self-assembly of the microgel monolayer, Π increases steadily until $\Pi \simeq 25\text{mN m}^{-1}$, where the sharp rise in the ex-situ curve indicates that the monolayer is nearing its maximum packing density before the buckling of the monolayer. At that value of Π, in-situ imaging becomes challenging as the microgels are tightly packed, causing the images to blur even by using fluorescent microgels [31, 32]. The main differences are visible when comparing directly the in-situ and ex-situ images at the same Π. Red- and black-framed images represent in-situ and ex-situ images, respectively. At low Π, both methods reveal microgels in hcp interacting through the portions adsorbed and stretched at the interface. As Π increases above $\simeq 22\text{mN m}^{-1}$, the in-situ an ex-situ monolayers show a different structure, since the in-situ images show still hcp order, while the ex-situ images show the typical clusters associated to the onset of the IPT. This clustering was attributed to the failure of the portions of the microgels stretched at the interface under lateral compression right at the liquid interface [24], leading to their collapse and causing that the microgels start to be in contact through their solvated portions in the sub-phase.

A quantitative analysis of the compression curves is provided in Figure 2. We track the microgel positions

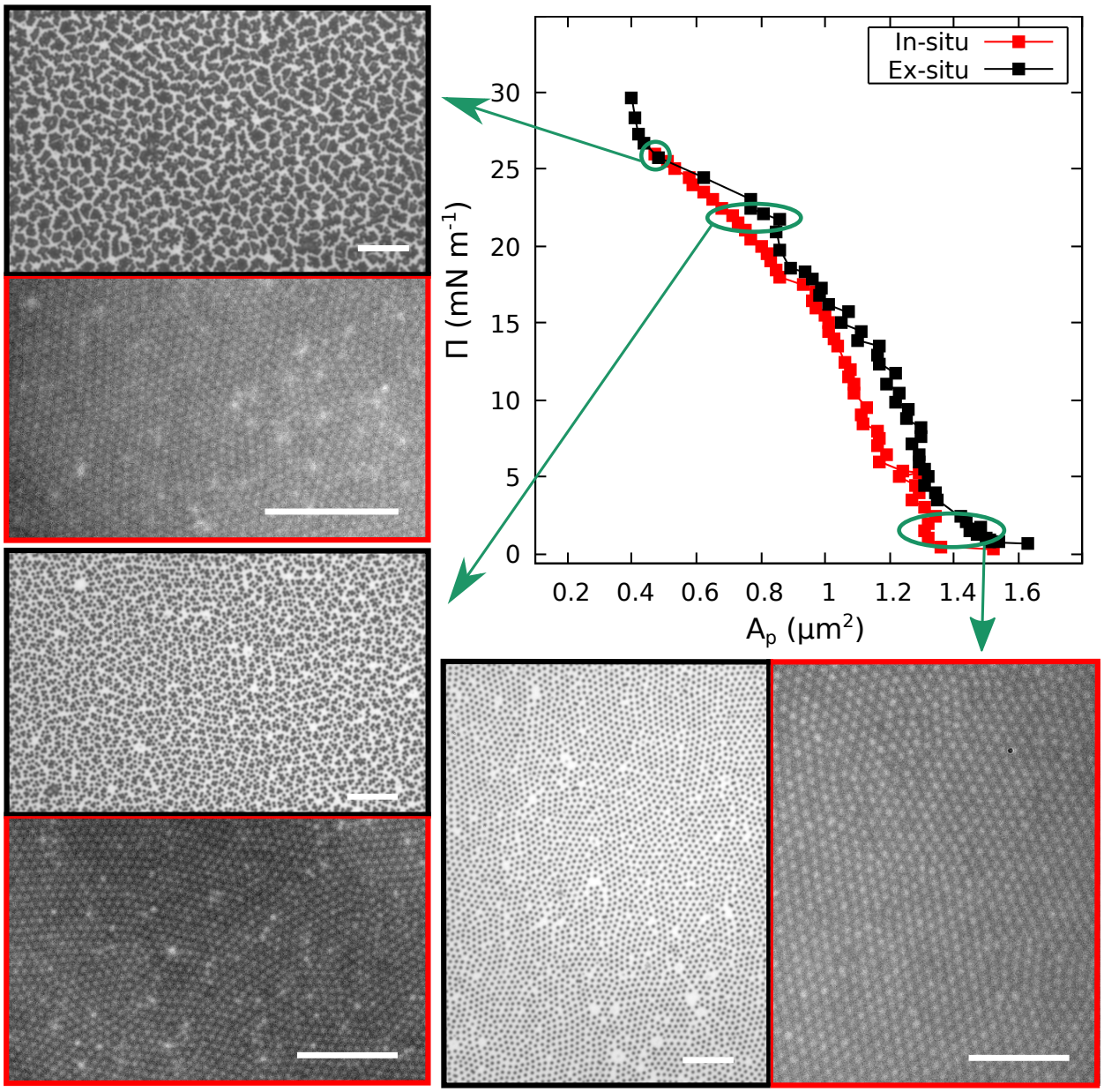

Figure 1: Surface pressure Π versus area per particle A_p of compression curves of the same pNIPAM microgel measured both in-situ with a microscope mounted on top of a Langmuir trough (■) and ex-situ after the deposition of the monolayer on a silicon wafer (■). The insets are representative images by optical microscopy with 10 μm scale-bars. Frames match the corresponding curve color.

in the in-situ and ex-situ images to show both the nearest neighbor distance (NND) and the order parameter ψ_6 vs Π, where $\psi_6 = 1$ indicates perfect hexagonal order. In the Supplementary Information we provide the same plots vs the microgels per area (A_p^{-1}, in Figure S1) to establish useful comparisons with previous studies [31, 32, 30]. The plots against Π provide a clearer picture about the state of the monolayer at each compression stage, enabling us to identify between different compression regimes. We start with the ex-situ curve since it reflects the usual behavior of a pNIPAM microgel monolayer deposited on a substrate [24]. At approximately $\simeq$ 18mN m^{-1}, the NND curve splits into two, marking the frontier of two distinct regions. In Regime I, the

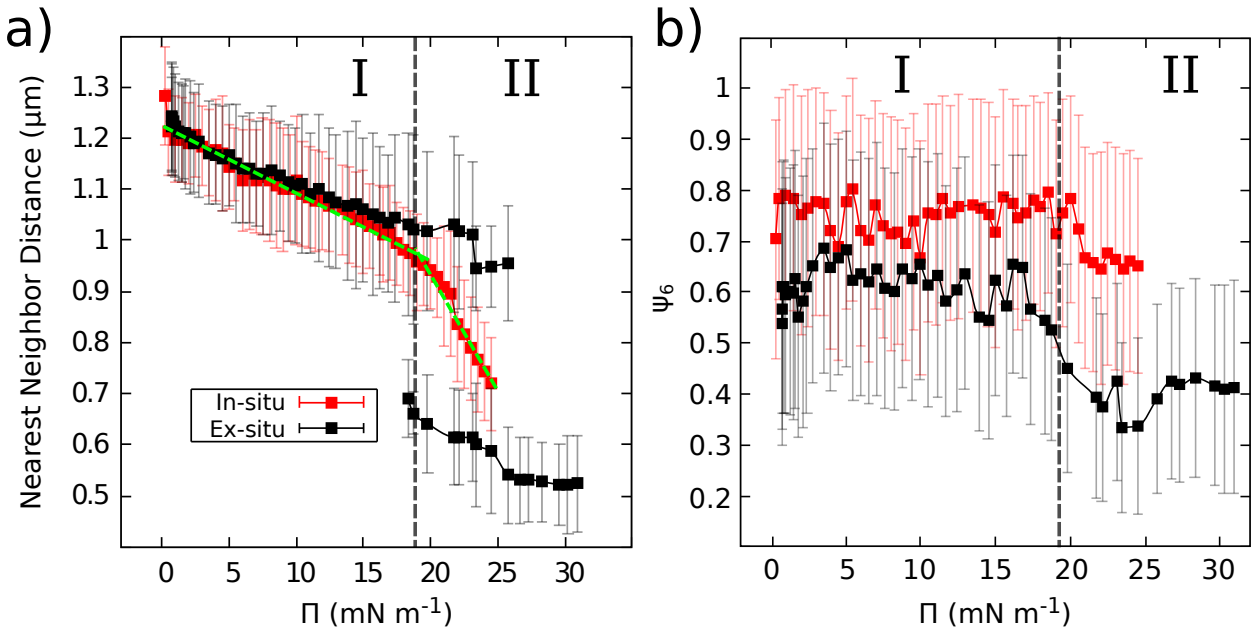

Figure 2: **a)** Evolution of the nearest neighbor distance of the microgel monolayer characterized ex-situ (■) and in-situ (■) vs Π. Roman numerals denote the different regimes at each compression stage. **b)** Corresponding order parameter ψ_6 for both curves in a). The dashed lines are guides to the eye.

NND decreases linearly with Π while microgels are assembled in hcp with all microgels in contact through their stretched portions at the interface. The frontier of Regime I and II is reached when the onset of the IPT occurs. In Regime II, some microgels experience the collapse of their stretched portions at the interface, resulting in microgels interacting through their solvated portions in the sub-phase, being this the cause of the curve split. It is worth noting that the onset of the IPT results in more space for the microgels and this reflects in a departure to higher values of NND for the top curve from the linear trend in Regime I. As Π increases, all microgels become in contact through their solvated portions in the sub-phase. Nevertheless, we do not reach Π values to recover a full hcp in Regime II, as we are interested in exploring the onset of the IPT, i.e. when, where, and why it starts to happen. The IPT is reflected in a drop in ψ_6 in Figure 2b. Now we compare with the in-situ measurements, revealing that the qualitative differences discussed in Figure 1 are quantitatively confirmed by the NND and ψ_6 plots. The in-situ curve shows a continuous reduction in NND without splitting but with a significant change in the slope, indicated by green dashed lines in the plot. This points out to a change in the compressibility of the microgels at approximately the same Π in which the onset of the IPT occurs for the ex-situ curve. This change in NND curve slope suggests that in Regime I the in-situ microgel monolayer is more difficult to be compressed than in Regime II. This is a direct result of the portions stretched at the interface being more rigid and difficult to compress against the surface tension. Once those stretched portions at the interface collapse, the microgels interact primarily by the softer solvated portions in the aqueous sub-phase [37]. This transition from Regime I to II also shows as a slight drop in ψ_6. By comparing the ψ_6 curves, the in-situ curve is consistently higher. Thus, transferring the monolayer onto a solid substrate not only induces the IPT but also decreases the overall ordering of the monolayer, even at low compression. Our findings are in agreement with latest works finding that the IPT does not seem to occur at the liquid interface but rather during the deposition of the monolayer [31, 32, 30].

Monolayer Behaviour at the Meniscus and Marangoni Effects

Since the IPT seems to occur during the deposition of the monolayer, we focus now on the behavior of the microgel monolayer at the meniscus generated on the solid substrate prior to the deposition. Nevertheless, studying the deposition process in-situ at the interface is non-trivial. Upon lifting the substrate to start transferring the monolayer, stick-slip may occur, altering the

conformation of microgels at the interface [38]. Also, the presence of a curved interface at the meniscus generates strong capillary forces that usually are responsible for the collapse of nanoparticle monolayers, with aggregation occurring at three-phases contact line, i.e. the solid substrate-liquid-air contact line [12]. Furthermore, the in-situ observation of the monolayer requires the use of a focused light spot, which might cause local heating and induce evaporation, i.e. light-induced Marangoni forces. Thus, it is worth exploring this rich behavior occurring at the meniscus, to elucidate if it contributes to the deposition-induced IPT. We set our next experiment at 23 mN m^{-1} to ensure being in Regime II according to Figure 2 and image the microgels at the receding meniscus in real time. When we start to rise the substrate across the microgel-laden interface, there is an initial stick of the meniscus. This was characterized by obtaining the meniscus profile while lifting the substrate, at different heights. The four profiles in Figure 3a illustrate how the meniscus evolves from a flatter profile (gray) to a steep curve (green). Further lifting of the substrate beyond the green profile resulted in the meniscus slip, beginning the deposition of the monolayer on the substrate. After this initial slip, the deposition process proceeded smoothly and steadily, without any further noticeable stick-slip effects, as observed in Movie M1 and Figure S2. This lack of stick-slip after the initial one might be due to the gelled and elastic nature of the microgel monolayer, and would be responsible for the usual homogeneous deposition patterns obtained by Soft Colloidal Lithography (SCL). The inset in Figure 3a shows that the microgels remained in hcp, similar to their configuration in the bulk of the interface as shown in the in-situ experiments in Figure 1, which we define as regions far from the meniscus where the interface is flat and thus capillary forces induced by the meniscus are negligible. To determine whether capillary forces at the meniscus contributed to the onset of the IPT, we examined the NND near the three-phases contact line and up to 15 mm away, significantly above the 2.9 mm capillary length of water/air interfaces. In Figure 3b, the NND is color-coded to match the corresponding meniscus profiles in Figure 3a. For the steeper menisci (purple and green curves), the behavior follows our expectations, since a curved interface induces capillary forces that tend to drive particles toward regions of greater curvature. These two curves show a decrease in NND near the three-phases contact line, indicating closer packing of microgels due to capillary forces, in comparison to the NND of 0.82 μm at the bulk interface, far away from the corresponding meniscus. As we move away from the three-phases contact line, the reduced curvature leads to weaker capillary forces and a corresponding increase in NND. The purple meniscus follows a similar trend to the green one with higher NND values because smaller curvatures result in weaker capillary forces. However, for the flatter menisci (blue and gray curves), we observed an unexpected increase of NND near the three-phases contact line, suggesting the presence of a repulsive force pushing microgels away from the meniscus and from each other. This unexpected behavior is an artifact of the in-situ optical microscopy, due to heating of the interface caused by the focused light used in our experiments. Such light-driven heating induces Marangoni flows, where a temperature gradient across the interface generates a surface tension gradient, creating a force directed from lower to higher surface tension regions [39]. In our experiments, Marangoni forces would act from the three-phases contact line towards the bulk interface, potentially explaining the expansion observed in the blue and gray meniscus profiles. To validate this hypothesis, we created a flat meniscus to eliminate capillary forces and measured the NND of the monolayer at the three-phases contact line under varying light intensities (correlating to different degrees of heating). These results were compared with those obtained using a non-absorbing glass substrate (see Figure S3 in SI), and only the more absorbing silicon substrate exhibited an increase in NND, dependent on light intensity, confirming that Marangoni stresses likely caused the observed unexpected increase in NND in Figure 3b.

While light-driven heating is not usually present when the monolayer is not observed in-situ in real time, this indeed constitutes a new light-driven tool to fine tune the interparticle distance of a microgel monolayer near the three-phases contact line and thus a fine tune of the interactions between the microgels at the monolayer. Thus, it is worth to further characterize it not only to better understand our system, but also to provide useful tools to take advantage of this effect. However, measuring the Marangoni force requires to determine with high precision the actual temperature along the meniscus. Experimentally, this could be done with complex techniques such as microscale thermometry, but due to the complex geometry of our experimental set-up, using this technique is not feasible [40]. To overcome this issue, we performed COMSOL simulations, described in detail in the Materials and Methods section, to determine the temperature gradients along the meniscus due to light heating. In this way, we can examine the balance between capillary forces, calculated from the menisci shapes, and Marangoni forces derived from the surface tension profile induced by heating. As shown in Figure 3c, simulated for the steeper meniscus in Figure 3a, heating at the three-phases contact line generates convective

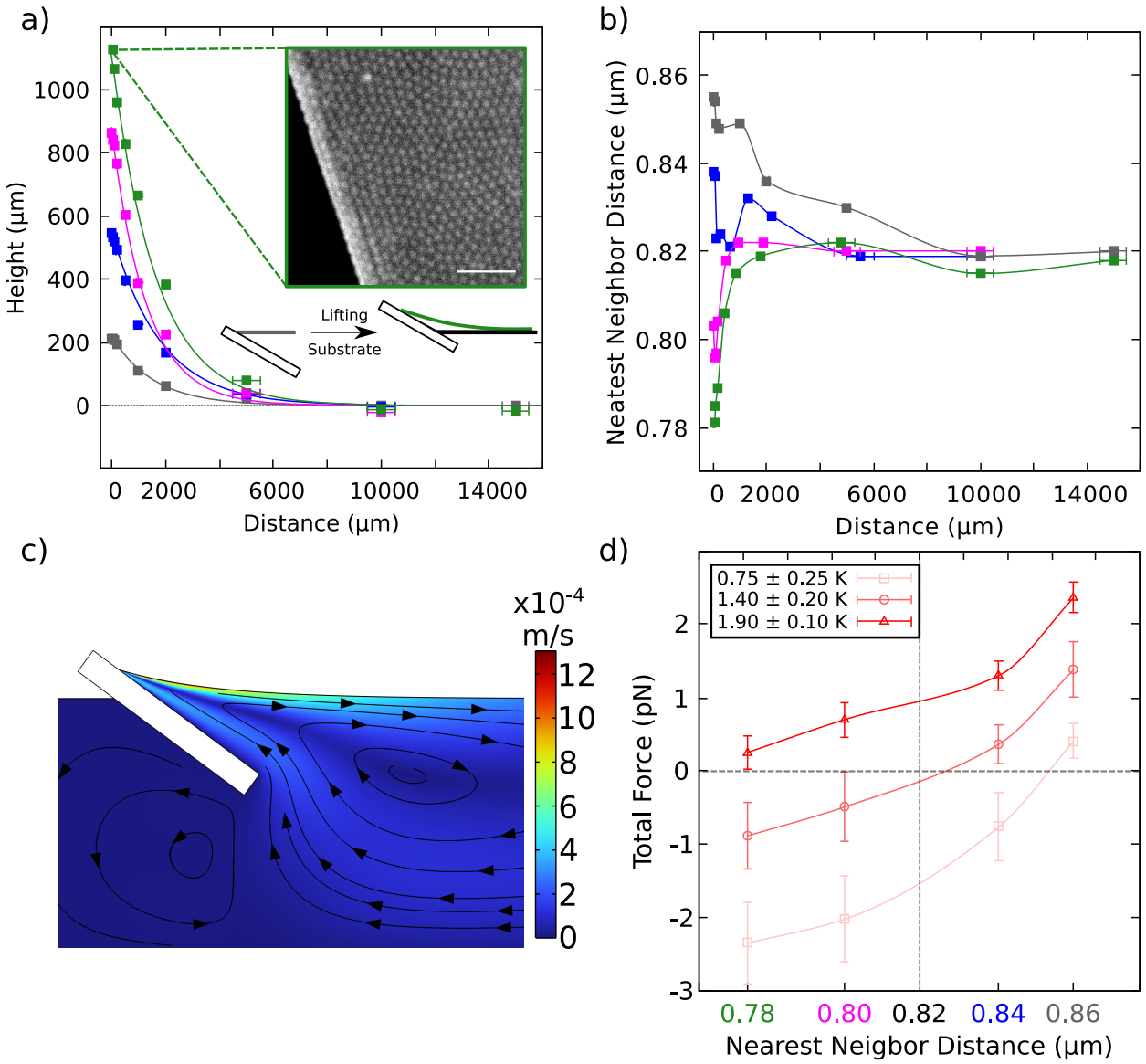

Figure 3: **a)** Evolution of the initial receding menisci shape upon raising the substrate across the interface. Each color represents a different meniscus profile during the same deposition process. The inset image shows the microgel monolayer near the three-phases contact line prior to the monolayer deposition. 5 μm-scale bar. The sketch represents the formation of the meniscus. Lines are theoretical fits to the experimental data based on Equation (4), taking into account the simulations that best fit the experiments. **b)** Nearest neighbor distances calculated at different positions along the menisci for each curve in a). Colors match the corresponding menisci profiles in a), and the lines are guides to the eye. **c)** Velocity field along the simulated experimental setup obtained via COMSOL for the green meniscus in a) for a temperature increase at the three-phases contact line of 1 K. The color map represents water velocity, while arrows indicate streamlines. **d)** Total Force obtained from theory and simulations as a function of the NND at the three-phases line of each menisci in panel b), with a color-coded x-axis matching the corresponding menisci. Calculations are performed at different temperatures ranges. The results are colored from light to dark red respectively corresponding to increasing heating. Horizontal and vertical dashed lines represents zero-force and the equilibrium NND at the bulk of the interface, respectively. Lines are guides to the eye.

flows at the interface and in the sub-phase. These forces are likely pushing the microgels at the interface away from the meniscus. In Figure 3d, we show the total force acting on a microgel as a function of the NND at the three-phases contact line for each meniscus in Figure 3a. This NND corresponds to the first point of each curve in Figure 3b, i.e. zero distance. The total force, detailed in the Theoretical Background section, presented corre-

sponds to the sum of capillary attraction corresponding to the four menisci, and the Marangoni repulsion, corresponding to a given temperature at the three-phases contact line. From light to dark red we show increasing temperatures in the simulations. The dashed horizontal and vertical lines indicate both zero force and the NND at the bulk of the interface, 0.82 μm, respectively. Points above the horizontal line correspond to scenarios dominated by Marangoni forces, where microgels are pushed away from the three-phases contact line, while points below correspond to capillary-dominated forces, pushing the microgels towards the three-phases contact line. Therefore, the best fit between experiments and simulations requires that the total force is negative on the bottom-left quadrant and positive on the top-right quadrant, with a continuous trend between the two. This happens for $\Delta T = 1.4 \pm 0.2\,K$. This is compatible with the difference of $\simeq 1\,K$ measured with an IR camera near the meniscus, relative to the bulk interface (see Figure S4 in SI). Our simulations, coupled with the experimental results, reveal that for a given temperature, the Marangoni force remains relatively constant, while capillary forces vary significantly due to curvature changes. As a result, the total force in Figure 3d decreases as the meniscus becomes steeper. Higher temperatures result in stronger Marangoni forces, shifting the total force curve upwards. This overall behavior is in good agreement with the experimental findings in which an increase in light intensity results in stronger Marangoni forces and thus an increase in the interparticle distance (see Figure S3 in SI). This exemplifies the light-driven fine tuning of the interparticle distance. Furthermore, the simulations also provide valuable insight about the order of magnitude of the forces acting at the interface. For example, at $\Delta T = 1.4 \pm 0.2\,K$ and flatter gray meniscus, the total repulsive force of around $1\,pN$ results in an NND increase of $\simeq 40\,nm$ respect to the NND at the bulk interface. For the steeper green meniscus, where the capillary attractive forces dominate, a total force of $-1\,pN$ results in a decrease of the NND of $\simeq 40\,nm$. Therefore, our simulations seem to be consistent with our experiments, since equal forces but of opposite sign affect the same way to the monolayer, increasing or decreasing the NND by a similar amount, in the single picoNewton range. The menisci profiles obtained from the simulations for $\Delta T = 1.4 \pm 0.2\,K$ are shown as solid lines in Figure 3a, showing that they closely match the experimental data, serving as a further validation of our model. Furthermore, a particular interesting result is that just by controlling the light intensity a "zero-force" can be obtained where the microgels are in the same effective regime as in the bulk interface. This controlled environment could offer new possibilities for studying fundamental interactions between microgels or other nanoparticles at fluid interfaces [41]. While very promising as a new tool to control the interaction between microgels at interfaces, the IPT can not be explained from the capillary forces caused by the meniscus curvature, regardless of using a non-absorbing substrate to "switch-off" the light heating-induced Marangoni force.

Drying of the Deposited Monolayer

Since the IPT does not occur at the meniscus near the three-phases contact line, the next step is to focus on the monolayer immediately after transfer to a solid substrate. As previously discussed, and shown in Movie M1, the transfer process is smooth and continuous. Initially, the monolayer is transferred while still covered by a thin water film. As shown in Figure 4a (and Movie M2), as the deposition continues the water film eventually recedes and the monolayer dries. It is during this "late" drying that the IPT seems to occur, with microgels collapsing into close contact. This reveals that the IPT takes place upon the drying of the water film that covers the deposited monolayer, an idea supported by a very recent work by Kuk et al. [42]. While we successfully identified when and where the IPT occurs, it remains necessary to determine why it occurs only above a certain Π threshold. We propose a simple theory to delve into the fundamental mechanics of the drying process. As shown in Figure 4b, during drying, capillary forces F_{cap} appear pushing microgels closer together. It is worth noting that while of the same nature, the source of this capillary force, which results from the drying of a liquid film between two adjacent microgels, is fundamentally different from the one discussed at the three-phases contact line in Figure 3, which resulted from the presence of a curved interface during the monolayer deposition. The main factor preventing the collapse of the microgels is their adhesion force F_{adh}, primarily determined by the interaction between the microgels and the substrate. The balance between these two forces determines whether the IPT will occur. If $F_{\mathrm{adh}} \geq F_{\mathrm{cap}}$ during drying, the microgels remain in place, and the IPT does not occur. Conversely, if $F_{\mathrm{adh}} \leq F_{\mathrm{cap}}$, the microgels will move and become in close contact, leading to the IPT.

Equation (1) provides the general expression for the F_{cap} during drying between two adjacent deposited nanoparticles [43]:

$$F_{\mathrm{cap}} = -\frac{2\pi\gamma Q_1 Q_2}{\mathrm{NND}}, \tag{1}$$

where γ is the surface tension of the water/air interface, NND is the separation between the two microgels, and

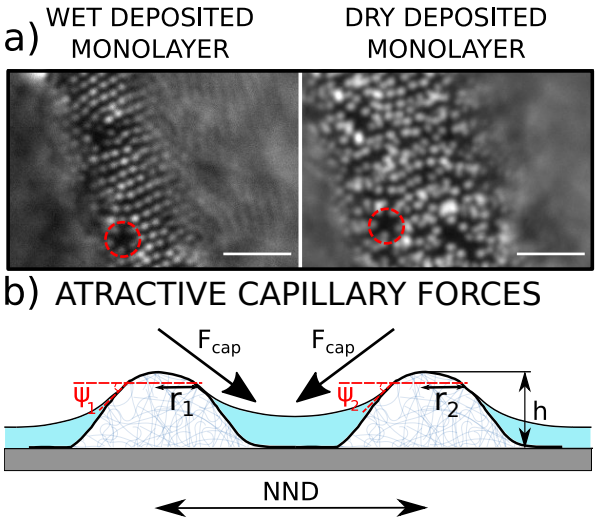

Figure 4: **a)** Optical microscopy images of microgel monolayer right after its deposition at $\Pi = 23\,\mathrm{mN\,m^{-1}}$, still wet with a thin water film (left) and after drying (right). 5 μm-scale bars.**b)** Schematic of the attractive capillary forces between two adjacent microgels during water film drying.

$Q_i = r_{\mathrm{cl},i} \sin\psi_{\mathrm{cl},i}$, where $r_{\mathrm{cl},i}$ is the radius of microgel i at the contact line (cl) with the interface and $\psi_{\mathrm{cl},i}$ is the contact angle between the meniscus and microgel i at the contact line. The negative sign reflects the attractive interaction between the two microgels. For two identical microgels, where $Q_1 = Q_2$, Equation (1) simplifies to:

$$F_{\mathrm{cap}} = -\frac{2\pi\gamma r_{\mathrm{cl}}^2 \sin^2\psi_{\mathrm{cl}}}{\mathrm{NND}}. \qquad (2)$$

Since for a chosen substrate and interface, F_{adh} and γ respectively are constant, and r_{cl} and ψ_{cl} are characteristics of the microgels that we can assume remaining nearly constant across all values of Π, the key variable that might change with increasing monolayer compression would be the interparticle distance NND. As Π increases NND decreases, and thus F_{cap} increases. Upon further compression, there is a critical Π at which the $\mathrm{NND} \leq \mathrm{NND_{min}}$, and thus $F_{\mathrm{cap}} \geq F_{\mathrm{adh}}$, being responsible for the onset of the IPT. This NND_{min} corresponds to the in-situ measured NND at the value of Π where the IPT first occurs in the experiments, $\mathrm{NND}_{in,IPT}$. From Figure 2a, this NND_{min} is found at a Π at which the change in the slope of the in-situ compression curve also occurs. Since at this Π the microgels interact trough their swollen parts in the aqueous subphase, it is reasonable to expect that they are close enough for the IPT to occur once deposited on the substrate. Nevertheless, while there seems to be a correlation between this change in the slope and the onset of the IPT, the IPT will occur once $F_{cap} > F_{adh}$. Therefore, varying F_{adh} by changing either the microgel or the surface chemistry of the substrate can indeed shift the onset of the IPT as shown in Figures S5a and S5c.

While measuring F_{adh} experimentally is challenging, we can provide an estimation based on the NND just before the IPT occurs. Once $\mathrm{NND_{min}}$ is known, we can estimate the F_{cap}. Given the Gaussian height profile of a deposited microgel, as shown schematically in Figure 4b, F_{cap} reaches its maximum at the base of the microgel, where r_{cl} is the largest. Regarding the contact angle, microgels are highly hydrophilic, leading to contact angles close to zero [27, 25, 44]. Therefore, as the water film recedes along the microgel height profile, the meniscus forms a contact angle that can indeed be approximated by the slope of the microgel height profile. We use here the height profile measured via AFM after drying of the monolayer since it is more representative of the drying process compared to the case of a fully hydrated microgel monolayer [21]. This slope, ψ_{cl}, can be estimated as $\psi_{\mathrm{cl}} = \tan^{-1}\left(\frac{h}{r_{\mathrm{cl}}}\right)$, where h is the height of the microgel. At the onset of the IPT, $F_{\mathrm{cap}} = F_{\mathrm{adh}}$, resulting in Equation 3.

$$F_{\mathrm{adh}} = F_{\mathrm{cap,IPT}} = \frac{2\pi\gamma r_{\mathrm{core}}^2 \sin^2\left(\tan^{-1}\frac{h}{r_{\mathrm{core}}}\right)}{\mathrm{NND}_{in,IPT}}. \qquad (3)$$

By experimentally measuring $\mathrm{NND_{min}}$, r_{cl}, and h, we can estimate the F_{adh}. Referring to Figure 2a, the IPT first occurred at $\simeq 18.5\,\mathrm{mN\,m^{-1}}$, where $\mathrm{NND_{in,IPT}} = 0.975\ \mu m$. On the other hand, r_{cl} and h can be measured by transferring the monolayer to a solid substrate and imaging it by atomic force microscopy. The resulting profile of the microgels is presented in Figure S6, from which we extracted the values of $r_{\mathrm{cl}} = 565$ nm and $h = 166$ nm. While h and r_{cl} during the drying of the wet monolayer may differ respect to the dry monolayer, the later are used as approximate values representative of the almost dry monolayer depicted in Figure 4b to obtain an estimation of F_{adh}. This estimated F_{adh} between the microgels and the substrate yields a value of $F_{adh} \approx 12$nN. This calculated value is in good agreement with adhesion forces in the nN range from more difficult and elaborate experimental measurements between alginate/Pnipam microgels and glass slides via colloidal probe microscopy [45, 46]. Therefore, our proposed model does not only captures the essential mechanism underlying the interplay between the capillary and adhesion forces upon drying of the microgel film, but also provides a novel and alternative method to estimate the

adhesion force between the microgels and the substrate. While this model estimates F_{adh}, this assumes that at the onset of the IPT $F_{adh} = F_{cap,IPT}$. Thus, changes in the microgel or substrate chemistry affecting either the F_{adh} or F_{cap} will shift the onset of the IPT depending on the balance of both forces [47, 42]. To test this, we deposited a monolayer of low crosslinked N-Vinylcaprolactam-based pVCL microgel, with 1% crosslinking density (see the SI for more details on their synthesis), both in regular and hydrophobic functionalized silicon substrates (see Figure S5). In that case, the onset of the IPT decreases from 15 to 12 mN m^{-1} when the substrate is hydrophobic. Since the proposed model mainly rely on the analysis of the compression curve of the microgel monolayer, it provides a much more accessible technique compared to colloidal probe. Furthermore, given that the adhesion between the microgels and a given substrate is expected to not vary substantially during the monolayer drying, our model effectively captures the reason why IPT occurs above certain surface pressures. This analysis shows that improving the adhesion between microgels and the substrate is a key parameter that can significantly enhance the homogeneity of the monolayer deposition, which is highly relevant also for all kind of nanoparticle monolayers for applications such as coatings, paints, and other surface treatments [5]. Since a recent study shows that functionalizing nanoparticles with polymers help to mitigate the coffee ring effect [5], we can infer that part of this effect might be due to an enhanced adhesion to the substrate. Regarding microgels, both tuning the crosslinking density of the microgels to make them softer and more adhesive, and tuning the wettability of the substrate, can enhance the adhesion forces, making it easier to achieve more ordered patterns and uniform depositions [48, 49, 42].

Developing an Alternative Deposition Method

Once we understand the mechanism behind the IPT during the deposition of microgel monolayers, we can suggest ways to avoid it, since certain applications may require maintaining microgels in a hcp with interparticle distances at which the IPT would typically occur. To achieve this, we developed an alternative deposition method that fully prevents the IPT. We reconsider Equation (3), where F_{adh}, h, and r_{core} are intrinsic to the microgels and the substrate, and thus the remaining tunable factor is γ. Lowering γ reduces F_{cap}, allowing microgels to get closer without collapsing due to the IPT. Nevertheless, using water/hexane instead of water/air to reduce γ from 72.5 to 50mN m^{-1} does not prevent the IPT [24, 50].

It is important to note that γ in Equation (3) corresponds to the interface of the wet deposited monolayer, which does not necessarily have to be the same interface at which the microgels were self-assembled and transferred from. Thus, we developed a new deposition method that minimizes F_{cap} by supercritical CO_2 drying. This approach allows the film to dry with $F_{cap} \simeq 0$. The method involves transferring the monolayer using a modified Langmuir-Schaefer deposition. In this process, the substrate is attached parallel and above the interface (see Figure S7), and is lowered until it contacts the interface. Once contact is established, the substrate is lifted. This approach addresses two critical issues: first, by placing the substrate in direct contact with the interface, the microgels are transferred from the bulk of the interface, avoiding any meniscus effects that could distort their conformation, as discussed before. Next, the rapid lifting, combined with the parallel orientation of the substrate, helps to retain a thin water film on the monolayer. The wet substrate is then stored in a Milli-Q water-filled Petri dish and prepared for supercritical CO_2 drying. The results of this method are shown in Figure 5d. It is worth noting that the method involves sequential steps replacing water by ethanol and by acetone before proceeding with the supercritical CO_2 drying.

To illustrate the method, we start with an in-situ microgel monolayer at 23 mN m^{-1}, where the dry ex-situ monolayer exhibits IPT, and its corresponding radial distribution function (RDF) in Figure 5a. The still wet deposited microgel monolayer in panel b) shows a monolayer structure that remains nearly identical after the deposition, with the radial distribution function (RDF) showing similar crystallinity in both cases. Although the in-situ recorded monolayer demonstrates slightly longer-range ordering, both the NND and ψ_6 are comparable between the two states. This confirms that the monolayer retains the properties it had at the interface, as long as it is kept wet. A comparison between the conventional deposition method and the Langmuir-Schaefer deposition combined with supercritical CO_2 drying is shown in Figures 5c and d, respectively. As discussed earlier in Figure 2, the conventional deposition method results in IPT at high Π, where microgels collapse into close contact. This is evidenced in Figure 5c, both visually and through the RDF, where an unfolded peak in the first maximum reflects two distinct ordering length scales: one of them corresponding to microgels in close contact, with two NNDs and a low ψ_6 value. In contrast, the monolayer deposited using our novel method combining a Langmuir-Schaefer deposition and supercritical CO_2 drying, shown in Figure 5d, closely resembles the conformation observed in Figures 5a and b. The RDF confirms

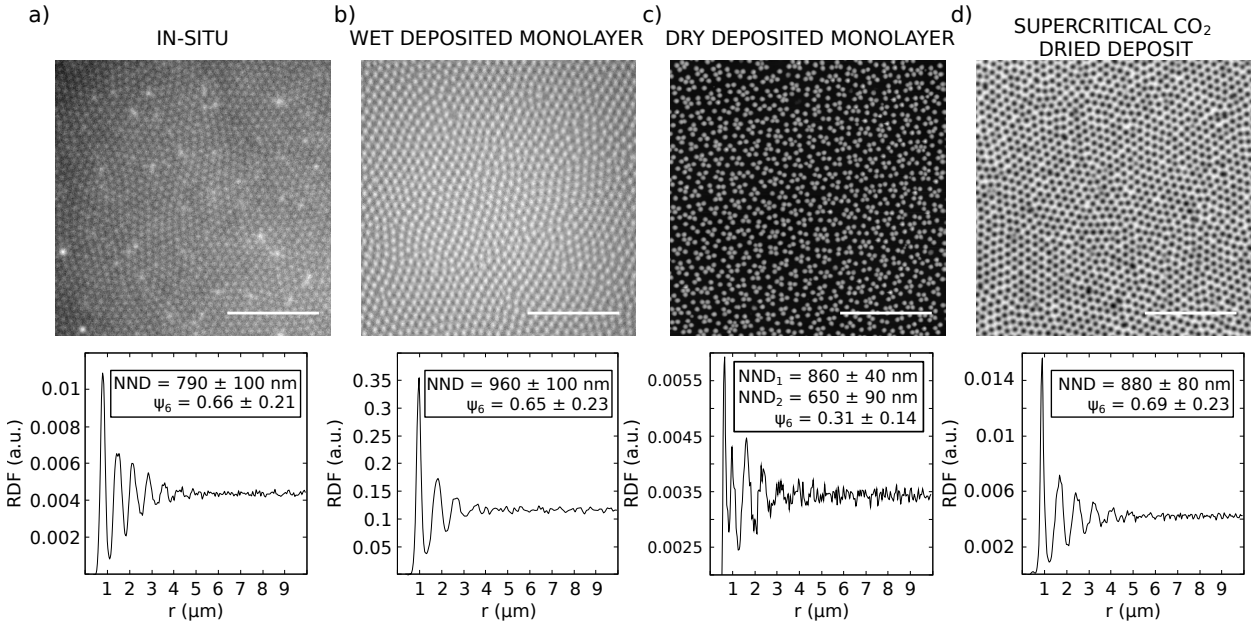

Figure 5: Optical microscopy images of a microgel monolayers at Π = 23 mN m^{-1} and corresponding radial distribution functions (RDF) with NND and ψ_6 values indicated. **a)** In-situ at the bulk interface, **b)** Ex-situ just after deposition, but still wet, **c)** Ex-situ as in b) after drying, exhibiting IPT, **d)** Ex-situ dry microgel monolayer with our novel technique combining a Langmuir-Schaefer deposition and supercritical CO_2 drying exhibiting no IPT. 10 μm-scale bars.

the long-range ordering seen in-situ at the interface, with a similar ψ_6 value compared with in the in-situ monolayer. This long range ordering is further confirmed by the iridescence patterns and large crystals aligned in the same direction (see Figures S8, S9 and Movie M3 in SI), and showing that these highly-ordered patterns can be achieved on cm^2 large substrates. We confirmed the homogeneity of the microstructures over whole substrates by evaluating the NND and ψ_6 at different locations on the same substrates (see Figure S10 in SI). It is worth noting that the slight changes in NND between the in-situ and the Langmuir-Schaefer deposited monolayer in Figure 6 might arise from slight differences in Π between experiments. This highlights the advantage of our novel method in preventing the IPT and maintaining the desired microgel arrangement. It should be noted that the Langmuir-Schaefer deposition method does not avoid the IPT without the subsequent supercritical CO_2 drying, as shown in Figure S11 in SI.

Finally, we reproduced the compression curve of Figure 2 to validate the effectiveness of our new method across a range of different Π values. In Figure 6, we present the compression curve of the microgel monolayer deposited via the Langmuir-Schaefer method and dried with supercritical CO_2 compared to the already discussed in-situ measurement. Both NND compression curves overlap almost entirely across all compression stages. Notably, while in-situ observations were limited to $\Pi \leq 26$ = mN m^{-1}, the new deposition method enables imaging the monolayer at all values of Π, reaching in our case up to 30 mN m^{-1}. The evolution of ψ_6, shown as an inset in Figure 6, reveals a slight decrease in hexagonal ordering for the deposited monolayer at low-to-medium surface pressures. Above Π = 23mN m^{-1}, the ordering significantly improves. We can compare the values of NND and ψ_6 before the IPT obtained by the Langmuir-Blodgett deposition and the Langmuir-Schaefer plus supercritical CO_2 drying in both Fig. 2 and 6. Thus, our novel methodology does not alter the arrangement of the microgels. Nevertheless, AFM analysis of the deposited monolayers revealed that this new methodology results in higher microgels as shown in Figure S12. This might be due to the supercritical drying, since the polymeric network might be less altered respect to the wet monolayer as we avoid capillary forces flattening the microgels during the drying. It is worth noting that the white spots observed at the highest Π in Figure 6 are microgels with lower crosslinking density, as can be seen in the AFM image in Figure S13 in the SI. Thus, our novel method effectively deposits the microgel monolayer while preserving the structure observed in-situ at the interface, avoiding all-together the IPT on cm^2 large

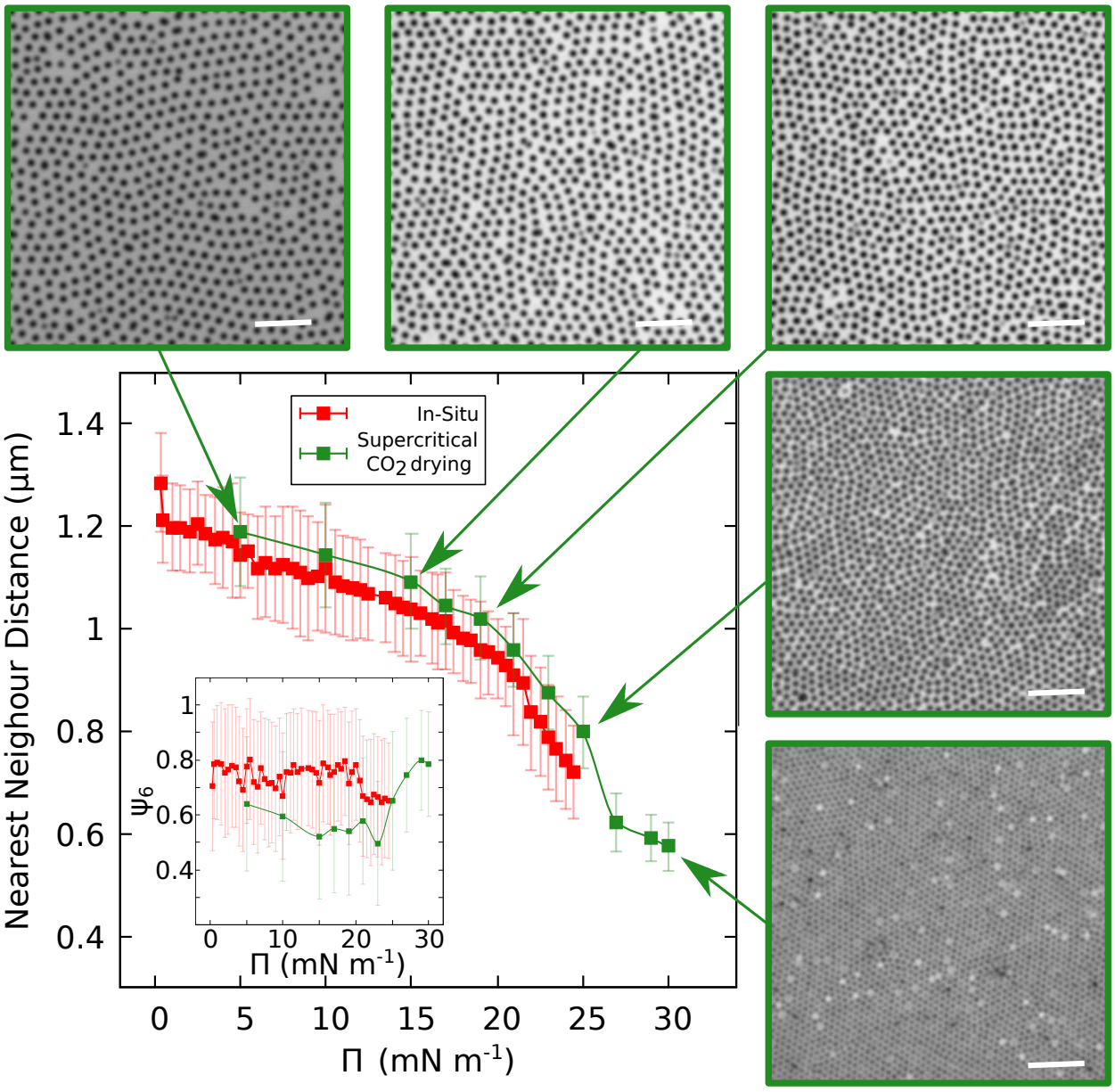

Figure 6: Nearest neighbor distance as a function of surface pressure Π for microgel monolayers observed in-situ at the interface (■), same as in Figure 2, and deposited on a solid substrate via the Langmuir-Schaefer method and dried with supercritical CO_2 (■). Lines are guides to the eye. Inset plot shows the corresponding order parameter ψ_6. Top rest of insets show microgel monolayers deposited at by our novel methodology up to Π = 30mN m^{-1}. 5 μm-scale bars.

substrates. In order to test the versatility of the Langmuir-Schaefer deposition plus supercritical CO_2 drying, we reproduced the results on monolayers obtained with the softer, i.e. 1% crosslinking density pVCL microgels. In Figure S5, we show that the lower adhesion between microgels and the hydrophobic substrates results in an onset of the IPT at lower Π compared to the regular hydrophilic substrates. Nevertheless, even in this scenario we avoid the IPT by using our new methodology.

Conclusions

In this study, we have analyzed the differences between in-situ and ex-situ characterization of self-

assembled microgel monolayers at liquid interfaces, identifying the conditions under which the isostructural phase transition (IPT) occurs, and have proposed a robust novel method to prevent the IPT.

The IPT has only been found in the deposited dry monolayers. While no collapse into close contact has been observed at the interface, a two-stage compression process was observed in-situ happening at the same Π where the IPT takes place for deposited dry monolayers. We have then investigated the rich behavior near the three-phases contact line, i.e the meniscus during the deposition. Although capillary forces at the meniscus were not responsible for inducing the IPT, they played a key role in influencing the monolayer conformation, reducing the NND in high-curvature menisci. In flatter menisci, light-driven Marangoni forces arising from in-situ observation of the monolayer dominated over capillary forces, pushing microgels away from the three-phases contact line. By successfully modeling this behavior through numerical simulations and theoretical calculations, we have demonstrated that light-driven Marangoni forces might be used to overcome capillary forces at the meniscus, creating a "zero-force" environment where the fundamental interactions of microgels and other nanoparticles can be studied. We have provided an estimation of the forces at the interface in the order of $\pm 1\ pN$ for a change of NND of $\pm 40\ nm$, respectively.

We have then examined the deposited but still wet monolayer, which preserved the structure observed in-situ at the liquid interface. Only upon drying the IPT took place. We have modeled this drying process and found that the IPT occurs when the capillary forces during drying exceed the adhesion forces between the microgels and the substrate. This analysis has revealed that the compression of the monolayer is necessary to achieve capillary forces larger than adhesion forces during the drying of a wet deposited monolayer. Nevertheless, the compression by itself is not sufficient, since we have not observed the IPT at the interface nor in wet deposited monolayers. Furthermore, we have estimated the adhesion force between the microgels and the substrate, providing an easy method to estimate its value from compression curves. This estimated adhesion force has been consistent with previous colloidal probe measurements, in the range of a few nanoNewtons.We have also demonstrated how tuning the surface chemistry can be used to modify the onset of the IPT. We reduced the adhesion between the microgel and the substrate by making it hydrophobic, shifting the IPT towards lower surface pressures.

After understanding the mechanism behind the IPT, we have developed a novel deposition method to avoid the IPT at any Π value. This method reduces capillary forces prior to the deposition by using a Langmuir-Schaefer deposition, in which we kept the substrate parallel to the interface, and eliminated capillary forces by using supercritical CO_2 drying. We have observed how this method increases the long-range ordering of the deposited monolayer, revealing iridescence patterns and large monocrystals on cm^2 large substrates. This method also successfully avoided the IPT in monolayers of softer microgels deposited either on regular or hydrophobic substrates. We have then presented a compression curve obtained with this novel deposition method and demonstrated its effectiveness in both preventing the IPT and replicating the in-situ behavior of the monolayer, even extending beyond the capabilities of the in-situ imaging and providing an actual ex-situ characterization method, effectively capturing the behavior of microgels at the interface.

We believe that these results will be of broad interest, since understanding the differences between in-situ and conventional ex-situ characterization methods provides the knowledge to choose an appropriate characterization technique tailored to the experimental conditions. Furthermore, understanding the mechanisms behind the IPT will aid in the design of new approaches to prevent it, such as the method that we have proposed and explored here, which is essential in fields requiring homogeneous deposition during drying. Our novel deposition technique might be potentially applied to other nanoparticles, such as core-shell or hollow microgels, or even hard nanoparticles functionalized with polymers.

Theoretical background

Capillary forces

When a liquid interface interacts with a substrate, a meniscus typically forms between the substrate and the interface. The characteristics of this meniscus depend primarily on the substrate/liquid affinity and the substrate morphology. If the substrate is perpendicular or tilted respect to the interface, the resulting meniscus will be macroscopic, with a characteristic capillary length specific to the interface. For the water/air interfaces, this capillary length is $\simeq 2.9\ mm$.

The shape of the meniscus can be described by the following equation [39]:

$$h(x) = \frac{L_c}{\tan\theta} \exp\left(-\frac{x}{L_c}\right), \tag{4}$$

where $h(x)$ is the meniscus height profile along the distance x from the three-phases contact line, L_c is the

capillary length, $\simeq 2.9\,mm$ in our case, and θ is the contact angle between the meniscus and the substrate.

When the meniscus forms, a pressure variation occurs along the interface, which is described by the Young-Laplace equation:

$$\Delta P = \gamma(\frac{1}{R_1} + \frac{1}{R_2}), \tag{5}$$

where γ is the surface tension and R_1 and R_2 are the principal radii of curvature. In our geometry, R_1 is the radius of curvature of the meniscus in the direction parallel to the interface (along x axis), while R_2 corresponds to the curvature along the flat three-phases contact line, i.e. $R_2 = \infty$.

Given the shape of the meniscus $h(x)$, the curvature C is defined as:

$$C = \frac{1}{R_1} = \frac{\left|h^{''}(x)\right|}{(1 + h^{'}(x)^2)^{3/2}}, \tag{6}$$

where $h^{'}$ and $h^{''}$ are the first and second order derivatives of the maniscus shape (4). Due to the pressure gradient within the meniscus, a nanoparticle at the interface experiences a force proportional to the product of the pressure and the nanoparticle area. Using the analytical expression for the meniscus from Equation (4), along with the experimentally determined size of our microgels, we derive the capillary force in the menicus $F_{cap,men}(x)$ as:

$$F_{cap,men}(x) = \frac{\pi(\frac{NND}{2})^2\gamma(x)}{L_c \tan\theta \exp(\frac{x}{L_c})(1 + \frac{1}{\tan^2\theta}\exp(-\frac{2x}{L_c}))^{3/2}}, \tag{7}$$

where NND can be substituted by the diameter of a microgel at the interface at a particular Π value.

Marangoni force

When a gradient in surface tension exists across an interface, a Marangoni force arise, generating convective flows directed toward regions of higher surface pressure [51]. This surface tension gradient can be induced by various factors, such as heating, evaporation, or changes in chemical composition [52, 53]. In our case, localized heating occurs when observing the interface with an optical microscope due to the highly focused light spot. This heating results in a force acting on the microgels during the observation of the monolayer, as described by [52]:

$$F_M(x) = A_m\frac{\partial\gamma}{\partial x}, \tag{8}$$

where $\frac{\partial\gamma}{\partial x}$ represents the surface pressure gradient along the interface, caused by the temperature gradient across the meniscus. We used COMSOL simulations to estimate the temperature profile and, subsequently, the variations in γ along the interface that best fit our experimental data.

Total Force

Taking into account both Capillary and Marangoni forces acting on a microgel, we define the total force F as

$$F(x) = F_{cap,men}(x) + F_M(x) \tag{9}$$

Materials and Methods

Materials

The pNIPAM microgels were synthesized by precipitation polymerization as described elsewhere [34, 14, 18]. Further details on the synthesis protocol and substrate functionalization can be found in the supporting information.

We purchased all reagents, N-isopropylacrylamide (NIPAM), N-methylenebisacrylamide (BIS), and potassium persulfate (KPS) from Sigma-Aldrich at analytical grade and used as received. We used isopropyl alcohol (Sigma-Aldrich, 99.8%) as a spreading agent for experiments conducted at the water/air interface. We cut silicon substrates of 2 x 1 cm^2 ($\langle 100\rangle$ orientation, p-type, Boron-doped, 1-10 Ω cm, University Wafer Inc., USA) by laser (Laser E-20 SHG II, Rofin, USA) and used for the deposition of microgel monolayers without further modification.

Physicochemical characterization

We characterized the hydrodynamic diameter (D_h) by Dynamic Light Scattering (DLS, ZetaSizer NanoZ, Malvern Instruments, UK). We performed the measurements at 25 and 50 °C to obtain the swollen and deswollen D_H of the microgels, respectively. We obtained the average, standard deviation, and PDI of three measurements. The PDI was determined by the Malvern ZetaSizer Software. We characterized the electrophoretic mobility (μ_e) at 25°C by Laser Doppler Electrophoresis (ZetaSizer NanoZ, Malvern Instruments, UK). For each characterization, we prepared a microgel solution of 0.1 wt% 15 minutes prior to each measurement. When the set temperature was achieved, the sample was stabilized during 3 minutes before starting the experiments.

In-situ observation of the microgel monolayer

For the in-situ observation and characterization in real time of the microgel monolayer we mounted an epi-fluorescent microscope (Nikon LV150) above a Langmuir trough (KSV NIMA, Biolin Scientific, Sweden), as shown in Figure S14. We prepared the microgel monolayer following the method described in our previous work [35]. We attached a silicon substrate to a motorized dipper, tilted at 30 °relative to the interface. The dipper was then lowered until half of the substrate was submerged below the interface. We filled the Langmuir trough with Milli-Q water, and placed a Wilhelmy plate in contact with the interface to measure the surface pressure Π. After waiting 10 min for the plate to become fully wet, we cleaned the interface by closing the barriers and aspirating the interface using a pipette tip and a vacuum pump. We repeated this cleaning routine until $\Pi \leq 0.3\,\mathrm{mN\,m^{-1}}$. Once we cleaned the interface, we created a microgel monolayer by spreading a microgel dispersion (4:1 water:isopropanol ratio) dropwise using a 100 μL glass microsyringe. We spread the microgels until $\Pi \simeq 0.7\ \mathrm{mN\,m^{-1}}$, after which the barriers were compressed to reach the desired Π. We made all the observations of the microgels using a super long working distance 100x objective (Nikon), providing a resolution of 0.065 μm/pixel.

To record the in-situ compression curve, we did observations in the *bulk* of the interface, sufficiently far from the walls and substrate to avoid capillary effects induced by menisci. We incremented Π in steps of $0.5\,\mathrm{mN\,m^{-1}}$, and we captured 50x50 and 100x100 $\mu\mathrm{m}^2$ images for subsequent analysis.

When studying the deposition process of a microgel monolayer on a silicon substrate in-situ, we observed the meniscus directly. We then compressed the interface to $23\,\mathrm{mN\,m^{-1}}$, since at this Π the collapse of the microgels into close contact already took place according to Figure 2. Starting at the three-phases contact line, where the silicon substrate, air, and water meet, we captured several images along the meniscus to record the monolayer behavior under different curvatures. Since the interface was tilted in these experiments due to the curved meniscus, we took multiple images at different focal planes and merged them into a single image to obtain 50x50 $\mu\mathrm{m}^2$ images. After recording the monolayer along a given meniscus, we slowly lifted the substrate at 0.1 mm/min to minimize disturbance at the interface, and we repeated the process to investigate the effect of different meniscus shapes on the microgel conformation. Finally, we recorded the deposition of the microgels by observing the receding meniscus at the three-phases contact line as we lifted the substrate.

After each experiment, we thoroughly cleaned the Langmuir trough by rinsing with tap water, followed by distilled water, wiping it with Kimtech paper and isopropanol, and then rinsing again with distilled water and finally with Milli-Q water.

Langmuir trough depositions

For the ex-situ characterization of the compression curve, the deposition process started by lifting the substrate while simultaneously closing the barriers. We carefully calculated the velocities of both the dipper and the barrier closure so that the entire length of the substrate, minus 1 mm, was lifted at the same time as the barriers were closed. At this point, we fully opened the barriers to induce a sudden change in Π, allowing later correlations between each position on the substrate and its corresponding Π.

We performed Langmuir-Schaefer depositions to prevent the isostructural phase transition (IPT) [24]. In these experiments, we mounted the substrate on a dipper parallel to the interface using an adapted holder, as shown in Figure S7. We prepared a microgel monolayer as previously described. We slowly lowered the dipper until the substrate touched the interface. Once contact was made, we rapidly lifted the substrate and removed it from the holder. This method left a thin water film on top of the deposited monolayer, preventing the microgels from drying. To avoid uncontrolled drying, we immediately stored the substrates in Milli-Q water. We subsequently dried the substrates using supercritical CO_2 to avoid the capillary forces during drying. For this, we followed the standard procedure used to dry biological samples. Briefly, we replaced the water in which the substrates were submerged with ethanol and then acetone before proceeding with supercritical CO_2 drying. During this liquid phase replacement it is important to avoid the drying of the substrate, as this leads to the IPT (see Movie M4). Once the substrate was immersed in acetone, it was transferred to the supercritical CO_2 dryer chamber (Leica EM CPD300), which was previously filled with acetone. After closing the chamber, we gradually substituted the acetone by liquid CO_2. Then, the temperature was set to 31 °C, where the CO_2 reached the supercritical point in the pressurized chamber. After this step, we removed the supercritical CO_2 from the chamber, which resulted in a dry substrate not subjected to capillary forces during drying (see Movie M4).

AFM and image analysis

Since the microgels deposited using the conventional method were too close due to collapse at high

Π (i.e., ≥ 22 mN m^{-1}), distinguishing them with the epi-fluorescent microscope was not possible. Therefore, we employed atomic force microscopy (AFM, motorized Dimension 3000) in tapping mode (Tap300Al-G cantilevers, 300 kHz, 40 N/m, BudgetSensors, Bulgaria) to analyze the monolayers at these higher Π. We acquired images with a resolution of 512x512 pixels^2 and a scan size of 30x30 μm^2 over the deposited microgel monolayer. We took an image every 500 μm along the substrate, enabled by a custom motorized AFM setup [54]. We then post-processed the images using Gwyddion software and converted to 16-bit grayscale.

Next, we analyzed the images using a customized particle tracking software based on the Python version of the publicly available TrackPy code by Crocker and Grier [55]. This allowed for precise localization of the center of each microgel, excluding microgels located at the image edges. We calculated radial distribution functions, g(r), and nearest neighbor distances. In addition, we computed the two-dimensional hexagonal order parameter, Ψ_6, using the following equation:

$$\Psi_6 = \left\langle \frac{1}{N_b} \left| \sum_{j=1}^{N_b} \exp\left(in\theta_j\right) \right| \right\rangle, \tag{10}$$

where N_b is the number of the nearest neighbors, n was set to 6 and θ_j is the angle between the particle and its nearest neighbor j.

To obtain the height of the deposited microgels, we used the software Gwyddion to create a mask which finds the maximum height of each microgel. This allowed us to find the height distributions of the microgels, fitting the data to a Gaussian distribution and obtaining the mean value from the mean of the fitted function. The error was calculated as the FWHM of the distribution.

COMSOL simulations

Imaging the meniscus with an infrared (IR) camera while simultaneously observing it through the optical microscope revealed that the light spot induced localized heating at the observation point on the meniscus, as shown in Figure S4. Due to the limitations of this technique, we performed COMSOL simulations to determine the temperature gradient along the meniscus and the resulting Marangoni flow caused by the surface tension gradient most probable to be compatible with the experimental results.

The problem was addressed using a 2D stationary model, with the meniscus shape modeled according to Equation (4). An example of the used geometry to simulate the green meniscus from Figure 3a is shown in Figure S15. An equivalent geometry was used for the other meniscus. We applied a no-slip boundary condition to the walls of the simulation box and the surface of the silicon substrate, while a slip condition was applied at the meniscus. We assigned the fluid properties to represent those of liquid water. We modeled the heating induced at the three-phases contact line due to in-situ observation by applying a heat-element at the three-phases contact line. We set the right wall of the simulation box to the water temperature from our experiments, ≃25 °C. We tested different temperature differences, ΔT, between the right wall and the heat element to study how varying light intensities affected the Marangoni force.

We used the non-isothermal flow multiphysics module in COMSOL to solve this problem, coupling the laminar flow of the liquid with heat transfer via conduction and convection. Given that temperature variations influence the velocity field, we incorporated the Boussinesq approximation into the Navier-Stokes equations. To account for the Marangoni effect, the following boundary condition was imposed [56]:

$$\vec{\mathbf{n}} \cdot \left[-\mathbf{pI} + \mu \left(\nabla \mathbf{u} + \nabla \mathbf{u}^T \right) \right] = -\gamma_T \nabla T, \tag{11}$$

where $\vec{\mathbf{n}}$ is the unit outward normal to the surface, p is the pressure, $\mathbf{I}$ is the identity tensor, μ is the dynamic viscosity of the water, $\mathbf{u}$ is the velocity vector, T is the temperature, and $\gamma_T = \frac{\partial \gamma}{\partial T}$ is the temperature derivative of γ, imported from the COMSOL materials library.

From the simulated γ profiles along the meniscus, we calculated the total force acting at the three-phases contact line as the sum of the capillary and Marangoni forces, according to Equations (7) and (8), respectively. The simulated meniscus profiles were then compared with experimental data to validate the model.

Author Contributions

Antonio Rubio-Andrés: Investigation, Data curation, Methodology, Validation, Visualization, Writing- Original draft preparation. **Delfi Bastos-González**: Conceptualization, Methodology, Resources, Supervision, Writing- Original draft preparation. **Miguel Angel Fernandez-Rodriguez**: Investigation, Conceptualization, Methodology, Software, Resources, Supervision, Writing- Original draft preparation, Project administration, Funding acquisition.

Supporting Information

Additional experimental results and details about the experimental setup.

Acknowledgments

We acknowledge the CIC from University of Granada for the CO_2 supercritical drying. This work was supported by the projects PID2020-116615RA-I00 funded by MCIN/AEI/ 10.13039/501100011033, and EMERGIA grant with reference EMC21_00008, and projects C-ING-208-UGR23, PY20-00241, A-FQM-90-UGR20 co-funded by Consejería de Universidad, Investigación e Innovación de la Junta de Andalucía, and by FEDER "Andalucía 2021-2027". Also by projects PID2023-149387OB-I00 and PID2023-147135OB-I00 funded by MICIU/AEI/10.13039/501100011033 and by FEDER, EU.

References

[1] K. Volk, J. P. Fitzgerald, P. Ruckdeschel, M. Retsch, T. A. König, M. Karg, Reversible tuning of visible wavelength surface lattice resonances in self-assembled hybrid monolayers, Advanced Optical Materials 5 (9) (2017) 1600971.

[2] M. Kolle, P. M. Salgard-Cunha, M. R. Scherer, F. Huang, P. Vukusic, S. Mahajan, J. J. Baumberg, U. Steiner, Mimicking the colourful wing scale structure of the papilio blumei butterfly, Nature Nanotechnology 5 (7) (2010) 511–515.

[3] N. Vogel, R. A. Belisle, B. Hatton, T.-S. Wong, J. Aizenberg, Transparency and damage tolerance of patternable omniphobic lubricated surfaces based on inverse colloidal monolayers, Nature Communications 4 (1) (2013) 2176.

[4] Y. Li, F. Piret, T. Léonard, B.-L. Su, Rutile tio2 inverse opal with photonic bandgap in the uv–visible range, Journal of Colloid and Interface Science 348 (1) (2010) 43–48.

[5] M. Rey, J. Walter, J. Harrer, C. M. Perez, S. Chiera, S. Nair, M. Ickler, A. Fuchs, M. Michaud, M. J. Uttinger, et al., Versatile strategy for homogeneous drying patterns of dispersed particles, Nature Communications 13 (1) (2022) 2840.

[6] W. Li, C. Zhang, Y. Wang, Evaporative self-assembly in colloidal droplets: Emergence of ordered structures from complex fluids, Advances in Colloid and Interface Science (2024) 103286.

[7] S. Hou, L. Bai, D. Lu, H. Duan, Interfacial colloidal self-assembly for functional materials, Accounts of Chemical Research 56 (7) (2023) 740–751.

[8] J. Zhang, Y. Li, X. Zhang, B. Yang, Colloidal self-assembly meets nanofabrication: From two-dimensional colloidal crystals to nanostructure arrays, Advanced Materials 22 (38) (2010) 4249–4269.

[9] S. Degand, G. Lamblin, C. C. Dupont-Gillain, Colloidal lithography using silica particles: Improved particle distribution and tunable wetting properties, Journal of Colloid and Interface Science 392 (2013) 219–225.

[10] R. McGorty, J. Fung, D. Kaz, V. N. Manoharan, Colloidal self-assembly at an interface, Materials Today 13 (6) (2010) 34–42.

[11] L. Teh, N. Tan, C. Wong, S. Li, Growth imperfections in three-dimensional colloidal self-assembly, Applied Physics A 81 (2005) 1399–1404.

[12] L. Isa, K. Kumar, M. Muller, J. Grolig, M. Textor, E. Reimhult, Particle lithography from colloidal self-assembly at liquid- liquid interfaces, ACS Nano 4 (10) (2010) 5665–5670.

[13] F. Grillo, M. A. Fernandez-Rodriguez, M.-N. Antonopoulou, D. Gerber, L. Isa, Self-templating assembly of soft microparticles into complex tessellations, Nature 582 (7811) (2020) 219–224.

[14] M. A. Fernandez-Rodriguez, M.-N. Antonopoulou, L. Isa, Near-zero surface pressure assembly of rectangular lattices of microgels at fluid interfaces for colloidal lithography, Soft Matter 17 (2) (2021) 335–340.

[15] F. A. Plamper, W. Richtering, Functional microgels and microgel systems, Accounts of Chemical Research 50 (2) (2017) 131–140.

[16] L. A. Lyon, A. Fernandez-Nieves, The polymer/colloid duality of microgel suspensions, Annual Review of Physical Chemistry 63 (1) (2012) 25–43.

[17] M. Rey, M. A. Fernandez-Rodriguez, M. Karg, L. Isa, N. Vogel, Poly-n-isopropylacrylamide nanogels and microgels at fluid interfaces, Accounts of Chemical Research 53 (2) (2020) 414–424.

[18] F. Camerin, M. A. Fernandez-Rodríguez, L. Rovigatti, M.-N. Antonopoulou, N. Gnan, A. Ninarello, L. Isa, E. Zaccarelli, Microgels adsorbed at liquid–liquid interfaces: A joint numerical and experimental study, ACS Nano 13 (4) (2019) 4548–4559.

[19] F. Pinaud, K. Geisel, P. Massé, B. Catargi, L. Isa, W. Richtering, V. Ravaine, V. Schmitt, Adsorption of microgels at an oil–water interface: correlation between packing and 2d elasticity, Soft Matter 10 (36) (2014) 6963–6974.

[20] N. Gnan, L. Rovigatti, M. Bergman, E. Zaccarelli, In silico synthesis of microgel particles, Macromolecules 50 (21) (2017) 8777–8786.

[21] M. Á. Fernández-Rodríguez, R. Elnathan, R. Ditcovski, F. Grillo, G. M. Conley, F. Timpu, A. Rauh, K. Geisel, T. Ellenbogen, R. Grange, et al., Tunable 2d binary colloidal alloys for soft nanotemplating, Nanoscale 10 (47) (2018) 22189–22195.

[22] D. Feller, M. Karg, Fluid interface-assisted assembly of soft microgels: recent developments for structures beyond hexagonal packing, Soft Matter 18 (34) (2022) 6301–6312.

[23] M. Rey, R. Elnathan, R. Ditcovski, K. Geisel, M. Zanini, M.-A. Fernandez-Rodriguez, V. V. Naik, A. Frutiger, W. Richtering, T. Ellenbogen, et al., Fully tunable silicon nanowire arrays fabricated by soft nanoparticle templating, Nano Letters 16 (1) (2016) 157–163.

[24] M. Rey, M. Á. Fernández-Rodríguez, M. Steinacher, L. Scheidegger, K. Geisel, W. Richtering, T. M. Squires, L. Isa, Isostructural solid–solid phase transition in monolayers of soft core–shell particles at fluid interfaces: structure and mechanics, Soft Matter 12 (15) (2016) 3545–3557.

[25] S. Bochenek, F. Camerin, E. Zaccarelli, A. Maestro, M. M. Schmidt, W. Richtering, A. Scotti, In-situ study of the impact of temperature and architecture on the interfacial structure of microgels, Nature Communications 13 (1) (2022) 3744.

[26] K. Zielińska, H. Sun, R. A. Campbell, A. Zarbakhsh, M. Resmini, Smart nanogels at the air/water interface: structural studies by neutron reflectivity, Nanoscale 8 (9) (2016) 4951–4960.

[27] J. Vialetto, S. N. Ramakrishna, L. Isa, In situ imaging of the three-dimensional shape of soft responsive particles at fluid interfaces by atomic force microscopy, Science Advances 8 (45) (2022) eabq2019.

[28] J. Vialetto, F. Camerin, S. N. Ramakrishna, E. Zaccarelli, L. Isa, Exploring the 3d conformation of hard-core soft-shell particles adsorbed at a fluid interface, Advanced Science 10 (28) (2023) 2303404.

[29] K. Geisel, L. Isa, W. Richtering, Unraveling the 3d localization and deformation of responsive microgels at oil/water interfaces: a step forward in understanding soft emulsion stabilizers, Langmuir 28 (45) (2012) 15770–15776.

[30] K. Kuk, V. Abgarjan, L. Gregel, Y. Zhou, V. C. Fadanelli, I. Buttinoni, M. Karg, Compression of colloidal monolayers at liquid interfaces: in situ vs. ex situ investigation, Soft Matter 19 (2) (2023) 175–188.

[31] T. Kawamoto, K. Yanagi, Y. Nishizawa, H. Minato, D. Suzuki, The compression of deformed microgels at an air/water interface,

Chemical Communications 59 (89) (2023) 13289–13292.
[32] T. Kawamoto, H. Minato, D. Suzuki, Relationship between π–a isotherms and single microgel/microgel array structures revealed via the direct visualization of microgels at the air/water interface, Soft Matter 20 (29) (2024) 5836–5847.
[33] S. Bochenek, A. Scotti, W. Ogieglo, M. A. Fernandez-Rodriiguez, M. F. Schulte, R. A. Gumerov, N. V. Bushuev, I. I. Potemkin, M. Wessling, L. Isa, et al., Effect of the 3d swelling of microgels on their 2d phase behavior at the liquid–liquid interface, Langmuir 35 (51) (2019) 16780–16792.
[34] M. A. Fernandez-Rodriguez, A. Martin-Molina, J. Maldonado-Valderrama, Microgels at interfaces, from mickering emulsions to flat interfaces and back, Advances in Colloid and Interface Science 288 (2021) 102350.
[35] A. Rubio-Andrés, D. Bastos-González, M. A. Fernandez-Rodriguez, Tuning the bulk behavior and 2d interfacial self-assembly of microgels by keggin-type polyoxometalate ionic specificity, Journal of Molecular Liquids 400 (2024) 124496.
[36] D. Feller, M. Otten, M. S. Dimitriyev, M. Karg, Non-close-packed plasmonic bravais lattices through a fluid interface-assisted colloidal assembly and transfer process, Colloid and Polymer Science (2024) 1–14.
[37] Y. Gerelli, F. Camerin, S. Bochenek, M. M. Schmidt, A. Maestro, W. Richtering, E. Zaccarelli, A. Scotti, Softness matters: effects of compression on the behavior of adsorbed microgels at interfaces, Soft Matter 20 (17) (2024) 3653–3665.
[38] C. Fuentes, M. Hatipogullari, S. Van Hoof, Y. Vitry, S. Dehaeck, V. Du Bois, P. Lambert, P. Colinet, D. Seveno, A. W. Van Vuure, Contact line stick-slip motion and meniscus evolution on micrometer-size wavy fibres, Journal of Colloid and Interface Science 540 (2019) 544–553.
[39] J. Sun, P. B. Weisensee, Marangoni-induced reversal of meniscus-climbing microdroplets, Soft Matter 19 (4) (2023) 625–633.
[40] L. Sixdenier, G. Baffou, C. Tribet, E. Marie, Quantitative microscale thermometry in droplets loaded with gold nanoparticles, The Journal of Physical Chemistry Letters 14 (49) (2023) 11200–11207.
[41] A. M. Luo, J. Vermant, P. Ilg, Z. Zhang, L. M. Sagis, Self-assembly of ellipsoidal particles at fluid-fluid interfaces with an empirical pair potential, Journal of Colloid and Interface Science 534 (2019) 205–214.
[42] K. Kuk, J. Ringling, K. Gräff, S. Hänsch, V. Carrasco-Fadanelli, A. A. Rudov, I. I. Potemkin, R. von Klitzing, I. Buttinoni, M. Karg, Drying of soft colloidal films, Advanced Science (2024) 2406977.
[43] P. A. Kralchevsky, K. Nagayama, Capillary interactions between particles bound to interfaces, liquid films and biomembranes, Advances in Colloid and Interface Science 85 (2-3) (2000) 145–192.
[44] L. Scheidegger, M. Á. Fernández-Rodríguez, K. Geisel, M. Zanini, R. Elnathan, W. Richtering, L. Isa, Compression and deposition of microgel monolayers from fluid interfaces: particle size effects on interface microstructure and nanolithography, Physical Chemistry Chemical Physics 19 (13) (2017) 8671–8680.
[45] N. Helfricht, E. Doblhofer, V. Bieber, P. Lommes, V. Sieber, T. Scheibel, G. Papastavrou, Probing the adhesion properties of alginate hydrogels: a new approach towards the preparation of soft colloidal probes for direct force measurements, Soft Matter 13 (3) (2017) 578–589.
[46] A. Mark, N. Helfricht, A. Rauh, M. Karg, G. Papastavrou, The next generation of colloidal probes: A universal approach for soft and ultra-small particles, Small 15 (43) (2019) 1902976.
[47] L. H. Alvarez, A. A. Rudov, R. A. Gumerov, P. Lenssen, U. Simon, I. I. Potemkin, D. Wöll, Controlling microgel deformation via deposition method and surface functionalization of solid supports, Physical Chemistry Chemical Physics 23 (8) (2021) 4927–4934.
[48] C. Picard, P. Garrigue, M.-C. Tatry, V. Lapeyre, S. Ravaine, V. Schmitt, V. Ravaine, Organization of microgels at the air–water interface under compression: Role of electrostatics and cross-linking density, Langmuir 33 (32) (2017) 7968–7981.
[49] M. Rey, X. Hou, J. S. J. Tang, N. Vogel, Interfacial arrangement and phase transitions of pnipam microgels with different crosslinking densities, Soft Matter 13 (46) (2017) 8717–8727.
[50] J. Vialetto, N. Nussbaum, J. Bergfreund, P. Fischer, L. Isa, Influence of the interfacial tension on the microstructural and mechanical properties of microgels at fluid interfaces, Journal of Colloid and Interface Science 608 (2022) 2584–2592.
[51] R. Van Gaalen, H. Wijshoff, J. Kuerten, C. Diddens, Competition between thermal and surfactant-induced marangoni flow in evaporating sessile droplets, Journal of Colloid and Interface Science 622 (2022) 892–903.
[52] J. Cejkova, M. Novak, F. Stepanek, M. M. Hanczyc, Dynamics of chemotactic droplets in salt concentration gradients, Langmuir 30 (40) (2014) 11937–11944.
[53] A. Nikkhah, S. Shin, Marangoni flows triggered by cationic-anionic surfactant complexation, Journal of Colloid and Interface Science 676 (2024) 168–176.
[54] J. G. Guerrero-Felix, J. Lopez-Miras, M. A. Rodriguez-Valverde, C. L. Moraila-Martinez, M. A. Fernandez-Rodriguez, Automation of an atomic force microscope via arduino, HardwareX 15 (2023) e00447.
[55] J. C. Crocker, D. G. Grier, Methods of digital video microscopy for colloidal studies, Journal of Colloid and Interface Science 179 (1) (1996) 298–310.
[56] S. H. Davis, Thermocapillary instabilities, Annual Review of Fluid Mechanics (1987) 403–435.